Research in Astron. Astrophys. **2009** Vol. **9** No. **10**, 1061–1077
http://www.raa-journal.org *http://www.iop.org/journals/raa*

***R**esearch in*
***A**stronomy and*
***A**strophysics*

The deep optical imaging of the Extended Groth Strip

Ying-He Zhao[1,2,3], Jia-Sheng Huang[2], Matthew Ashby[2], Giovanni Fazio[2] and Satoshi Miyazaki[4]

[1] Purple Mountain Observatory, Chinese Academy of Sciences, Nanjing 210008, China; *yhzhao@pmo.ac.cn*
[2] Harvard-Smithsonian Center for Astrophysics, 60 Garden Street, Cambridge, MA 02138, USA
[3] Department of Astronomy, Nanjing University, Nanjing 210093, China
[4] National Astronomical Observatory of Japan, Mitaka, Tokyo 181 – 8588, Japan

Received 2009 April 29; accepted 2009 May 24

Abstract We present $u'g'R$ optical images taken with the MMT/Megacam and the Subaru/Suprime telescopes of the Extended Groth Strip survey. The total survey covers an area of about ~ 1 degree^2, including four sub-fields and is optimized for the study of galaxies at $z \sim 3$. Our methods for photometric calibration in AB magnitudes, the limiting magnitude and the galaxy number count are described. A sample of 1642 photometrically selected candidate Lyman-Break Galaxies (LBGs) to an apparent $R_{\rm AB}$ magnitude limit of 25.0 is presented. The average sky surface density of our LBG sample is $\sim$1.0 arcmin $^{-2}$, slightly higher than the previous finding.

Key words: galaxies: high-redshift — galaxies: photometry — surveys

1 INTRODUCTION

When and how galaxies formed is one of the primary questions in astronomy today. Observations of young galaxies at high redshifts are a straightforward approach to solving this problem. Taking advantage of the progress in observation technology and also sophistication of selection methods (e.g., color selection, Steidel & Hamilton 1993; Steidel et al. 2003; Franx et al. 2003; Daddi et al. 2004), multicolor surveys allow for the location of high redshift galaxies. Among the various methods, the Lyman break dropout technique (Steidel & Hamilton 1993), sensitive to the presence of the 912 Å break, is designed to select $z \sim 3$ galaxies; it has successfully been used to find many young star-forming galaxies beyond $z \sim 2$ (e.g., Steidel et al. 2003; Lehnert & Bremer 2003; Ouchi et al. 2004; Dickinson et al. 2004; Sawicki & Thompson 2006).

Since their first discovery in the 1990s, various properties of Lyman Break Galaxies (LBGs) have been extensively studied (e.g. the luminosity function and the clustering property). However, the stellar mass, which is a robust tool to probe galaxy evolution, has been estimated only based on ground-based photometry. For high redshift galaxies, this only samples out to the rest-frame optical band. The observed luminosity at these wavelengths is dominated by recent star-formation activity rather than the stellar population that has accumulated over the galaxy's lifetime. With the advent of the Spitzer Space Telescope (hereafter Spitzer, Werner et al. 2004), we can probe the rest-frame near-infrared (NIR; z, J, H, K) band (for $z \sim 3$ galaxies) where the light is more sensitive to the total stellar mass, which is dominated by lower mass stars. In addition, longer wavelengths are less affected by dust extinction that may strongly attenuate ultraviolet light. Shapley et al. (2005) showed that the addition of Spitzer IRAC

(Fazio et al. 2004) data reduces stellar mass uncertainties by a factor of 1.5–2 relative to estimates based on the optical-K_s photometry alone, for their LBG sample of $z \sim 2$. Elsner et al. (2008) found that the stellar mass is overestimated by more than a factor of three on average for $z \sim 3$ galaxies without Spitzer data.

Huang et al. (2005) have shown that, at limiting flux densities (5σ) of 0.5 μJy at 3.6 and 4.5 μm, and 2.7 μJy at 5.8 and 8.0 μm, the detection rates for $z \sim 3$ LBGs are about 83%, 78%, 21% and 17% at 3.6, 4.5, 5.8 and 8.0 μm, respectively. Preliminary results of adding IRAC photometry to stellar mass estimates have been presented in e.g. Barmby et al. (2004), Rigopoulou et al. (2006) and Huang et al. (2007) for $z \sim 3$ LBGs.

In spite of the stellar mass of LBGs, we can also use the Spitzer deep mid- and far-infrared (MIPS; Rieke et al. 2004) data to study the link between UV-selected LBGs ($\sim$5% detections in MIPS imaging data, Huang et al. 2005) and infrared-selected Ultra Luminous Infrared Galaxies (ULIRGs) at high redshifts. To take advantage of the deep Spitzer IRAC+MIPS imaging data to study the physical properties and evolutionary processes of galaxies at redshift ≥ 3, we began our optical imaging of the Extended Groth Strip (EGS: $\alpha = 14^{\rm h}17^{\rm m}$, $\delta = +52^{\circ}30'$) sky field using the MEGACAM on the MMT (u'- and g'-band) and the Subaru telescope (R-band). The EGS region is an extension of a *Hubble Space Telescope (HST)* survey, which consists of 28 Wide-Field Planetary Camera 2 (WFPC2) pointings carried out in 1994 by the WFPC team (Rhodes et al. 2000). This field benefits from low extinction, low Galactic and zodiacal infrared emission and has attracted a wide range of deep observations at essentially every accessible wavelength (e.g. the All-Wavelength Extended Groth Strip International Survey, AEGIS; Davis et al. 2007). Although the ongoing Canada-France-Hawaii Telescope Legacy Survey (CFHTLS) [1] has carried out optical imaging observations, there are three things that we need to improve: (1) our u' filter cuts at 4000 Å on the red side, which is about 200 Å blueward of their u' filter. The u'/g' filter combination is optimally placed for measuring the Lyman continuum break in galaxies at $z \sim 3$; (2) their survey only covers about half the area of the Spitzer data set; and (3) their observations are not very deep (as in Sect. 3.1).

This paper is organized as follows. In Section 2, we present a brief description of the observations and data pre-reductions. We also describe the method of photometric calibration (e.g. magnitude zero points, the estimate of the sensitivity of the mosaics) in this section. We present the results of galaxy number counts at the $u'g'R$ bands, and present a photometrically selected LBG sample at $z \sim 3$ in Section 3. In the last section, we present a summary for this paper.

2 OBSERVATION AND DATA REDUCTION

The imaging data for the four sub-fields presented here were obtained on the MMT and Subaru telescopes during 2005, detailed in Table 1. The imaging filters used were the SDSS $u'g'$ and the Johnson-Cousins R system. The filter system passbands are shown in Figure 1, with the $U_nG\mathcal{R}$ system (Steidel et al. 2003) superposed. Our u' filter is identical to the U_n filter. The g' filter has a similar effective wavelength to G but is wider. The R filter is shorter and slightly narrower than the $\mathcal{R}$ filter. This is the main cause of the difference of the source colors between these two filter systems.

In general, individual integrations of 340 – 500 (u') and 600 or 1200 (g') seconds were obtained by using the MMT/Megacam with a pixel scale of 0.08″. The R-band images were conducted by the Subaru/Suprime-Cam (Miyazaki et al. 2002) with a pixel scale of 0.202″. Total integration times varied depending on observing conditions, filters and telescope/camera combinations.

The data reduction for the u'- and g'-band images, such as making bias and flat corrections, mosaics, flux and astrometrical calibrations, was carried out by Ashby, and we will only give a brief description here. The details of these procedures can be found at Ashby's homepage [2]. For the R-band images, please refer to Miyazaki et al. (2002) and Miyazaki et al. (2007) for detailed data reduction procedures.

[1] see *http://www1.cadc-ccda.hia-iha.nrc-cnrc.gc.ca/community/CFHTLS-SG/docs/cfhtls.html*

[2] *http://www.cfa.harvard.edu/∼mashby/megacam/megacam_frames.html*

Table 1 Journal of Optical Observations of EGS

Field	α (J2000.0)[a]	δ (J2000.0)[a]	Filter	Telescope	Seeing (arcsec)	Zero point (mag)
0	14 16 00.84	+52 11 59.1	u'	MMT	0.84	31.01
			g'	MMT	1.0	33.53
			R	Subaru	0.70	31.923
1	14 18 07.85	+52:35:34.8	u'	MMT	1.08	30.95
			g'	MMT	1.33	33.50
			R	Subaru	0.60	31.881
2	14 20 18.44	+52 59 11.0	u'	MMT	0.95	31.44
			g'	MMT	1.41	33.83
			R	Subaru	0.70	31.860
3	14 22 30.83	+53 22 51.0	u'	MMT	0.88	31.13
			g'	MMT	1.60	34.57
			R	Subaru	0.72	31.911

a: Positions of the field centers. Units of right ascension are hours, minutes and seconds, and units of declination are degrees, arcminutes and arcseconds.

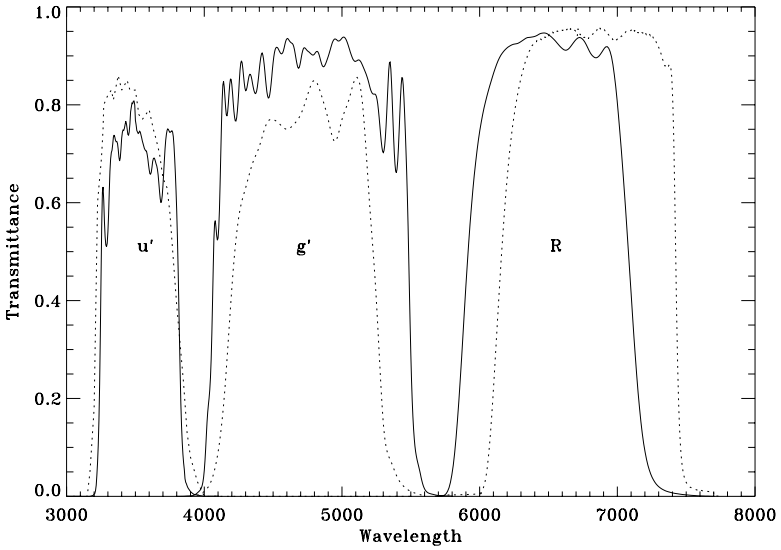

Fig. 1 Filter system used for the deep imaging, u' (3500/600), g' (4750/1500) and R (6500/1200). The dotted line shows the filter system which is used by Steidel et al. (2003).

In brief, after CCD processing, the images were astrometrically calibrated with reference to the USNO-B1.0 astrometric catalog (Monet et al. 2003), using a polynomial solution to map the focal plane to the astrometric reference. The resulting accuracy is better than $0.2''$.

The twilight flats at u' and g' are somewhat contaminated by OH skyglow emission that can sneak in to varying degrees depending on the distance from the center of the megacam FOV. Therefore, we need to correct for the OH contribution to the twilight flat before flux calibrations. The OH contamination was compensated for by observing a part of our field (F1) during photometric conditions at a number of positions with short exposures (60 s) intended to match the depth of the SDSS survey. We then used the multiple observations of stars in those short integrations to correct the contaminated flat by measuring the variation in apparent brightness of those stars with respect to their distance from the MMT boresight.

The corrections thereby derived were applied to all individual Megacam frames before we constructed our coadds. Then, we generated the catalogs by running SExtractor (Bertin & Arnouts 1996) on the images, and then computed the zeropoint for each image by position-matching these catalogs to the SDSS (Gunn et al. 1998) catalogs for the same field. In Table 1, we also list the resulting magnitude zero points for these images. The magnitudes in this paper are all given in AB magnitudes (Oke & Gunn 1983; Fukugita et al. 1996).

The calibrated images were coadded using SWarp written by E. Bertin of Terapix, and then were combined as full mosaics using the IRAF[3] task *imcombine*. The mosaics of u'- and g'-band images have a pixel scale of $0.318''$, larger than that of the R-band images. We rebinned and rotated the R-band images to match the u'- and g'-band images, in order to obtain the color information of each source in the image by using SExtractor's double-image mode. The process of rebinning will cause a change of –0.98 $[\equiv -2.5\log_{10}(0.318/0.202)^2]$ mag in the R magnitude zero point.

In order to have a good estimate of the observational qualities for each field and filter, we run SExtractor version 2.5 on each image individually, not the rebinned image, to generate the photometric catalog. The magnitudes used for further analysis are all measured in Kron-style apertures (SExtractor's MAG_AUTO), except for the section of LBG selections. These should give good estimates of the total magnitudes for each source, especially for the stars.

Stellar color is a useful diagnostic to examine the photometric magnitude zero-point. Stars occupy a relatively constrained locus in the color-color space. Any offsets between the observed and synthetic colors indicate a zero point error. This test can be applied to our four fields, which lie in the SDSS (Gunn et al. 1998) field.

2.1 Stellar Color-Color Diagram

In Figure 2, we illustrate the selection of stars. The plot shows the half-light radius plotted versus magnitude. In this figure, the stars show up as a well defined horizontal locus while the galaxies occupy a range of magnitudes and radii. The upturn at the bright end indicates the sources are saturated. The pink points indicate the cuts in magnitude and radius to select stars for further analysis.

Figures 3, 4 and 5 show color-color diagrams for stars both in the EGS and SDSS fields, for u'-, g'- and R-bands, respectively. The magenta triangles and solid circles in each figure represent synthetic and observed colors, respectively. The different panels in each figure are different fields. The synthetic colors are obtained using the observed stellar spectra library HILIB (Pickles 1998) to be convolved with the transmission curve of the filters. Since we do not get the response curve, we do not apply the CCD quantum efficiency (QE) for MMT/Subaru filters during this calculation. However, the results of synthetic colors show good agreement with the observed colors, except for a small systemic offset of ~ 0.05 mag in the diagram for g'-band images. This offset may be due to: 1) the effect of the CCD QE curve; 2) the errors of magnitude zero points. However, the CCD QE curve on the g' filter is fairly flat, and the effect of QE should be canceled out in the resulting g' magnitude. Hence, the offset is most likely a zero point error.

In order to investigate further, we plot the synthetic and observed $(g'-r')$ vs $(u'-g')$ for SDSS filters in Figure 6. We can see that these plots are very consistent with those in Figure 3. This indicates that the effect of CCD QE is very tiny. Therefore, we conclude that the offsets between the synthetic and observed colors are caused by the zero point errors.

We do NOT use SDSS u' and g' magnitudes to do the plots in Figure 5. The reason is that the stars selected from the R-band images are too dim to acquire accurate magnitudes from SDSS catalogs. However, there are no visible offsets between the observed and synthetic colors after we corrected the errors of the g'-band zero points.

[3] IRAF is distributed by the National Optical Astronomy Observatory, which is operated by the Association of Universities for Research in Astronomy, Inc., under cooperative agreement with the National Science Foundation.

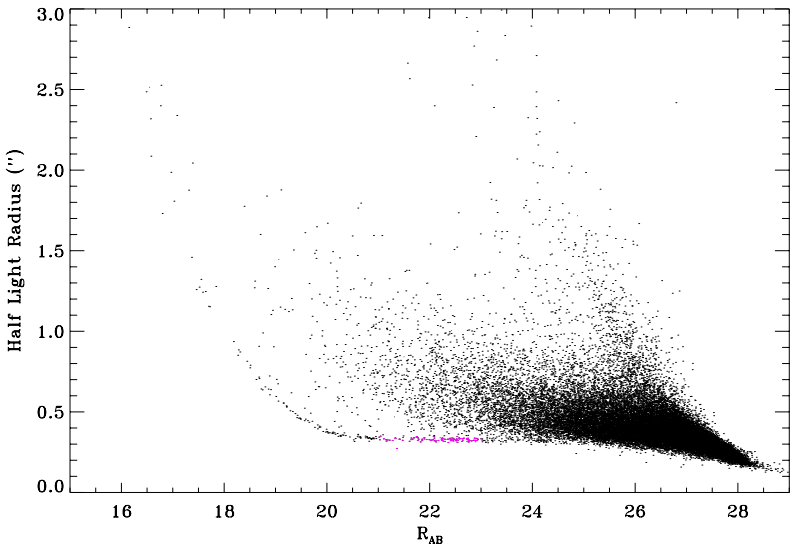

Fig. 2 Half-light radius plotted versus total magnitude. The horizontal branch shows the locus of the stars. The upturn at the bright end indicates the sources are saturated. The pink points (see electronic version) are the conservative cuts in magnitude and radius to select stars for further analysis.

2.2 Limiting Magnitudes

The sensitivities of the mosaics were tested using a Monte-Carlo procedure. Large numbers of fake point-like sources are added to the images and then we try to recover them using the same parameters as those used to generate the real image catalogs. The positions of the artificial sources are assigned randomly apart from the requirement that they are at least one aperture diameter away from the detected sources.

In Figure 7, we show the recovery rates plotted versus magnitudes for the four u'-band images. We can see that the image of Field 0 is the deepest, while Field 3 is the shallowest. The limiting magnitudes of these four fields are $\sim$26.8, 26.6, 26.5 and 26.1 mag, by using 80% completeness level as the criterion. We will find that these results are consistent with those given by the galaxy number counts.

Figure 8 shows the simulation results for g'-band images. The scatter, even at the bright end, is much larger than the other two band images. The large variation in seeing is likely responsible. The limiting magnitudes are $\sim$26.7, 25.7, 25.8, 25.2 mag.

The R-band results are shown in Figure 9. As far as we know, this band has the best image qualities, reflected by the small scatter and high recovery rate. The limiting magnitudes are $\sim$ 26.2, 26.4, 26.3 and 26.3 mag.

3 RESULTS AND ANALYSIS

3.1 Galaxy Number Counts

Galaxy number count is a useful tool for obtaining the depth and homogeneity of the survey, and also for constructing galaxy evolution models. In the following, we present the galaxy number counts in the u'-, g'- and R-bands. The number counts are constructed for the deep central field in the four subfields first, and only tiny variances among these four fields are found. Then, we take the mean values as the resulting counts. The total areas are $0.25\,\mathrm{deg}^2$, $0.10\,\mathrm{deg}^2$ and $0.20\,\mathrm{deg}^2$, for the u'-, g'- and R-bands, respectively. When doing the counts, no dereddening was applied.

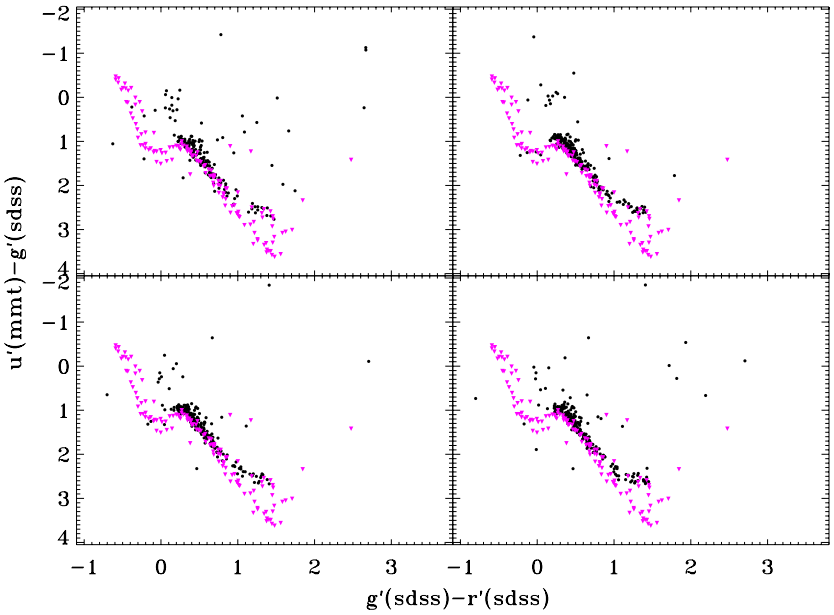

Fig. 3 Color-color diagram for u'-band images. The four panels correspond to the four different fields. *Upper left*: Field 0; *Upper right*: Field 1; *Lower left*: Field 2; *Lower right*: Field 3. We can see great consistency between the observed (*black circles*) and synthetic (*magenta triangles*; see electronic version) colors, which indicates that the magnitude zero points are correct.

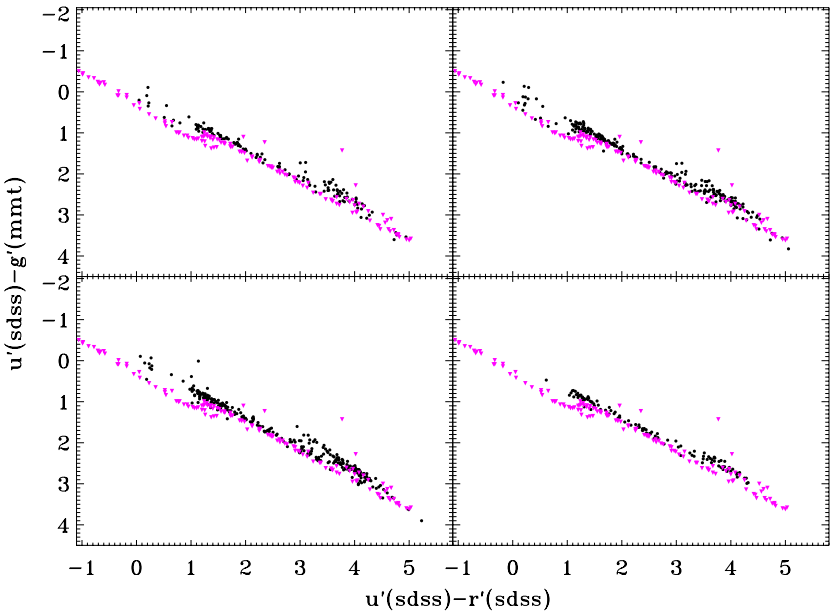

Fig. 4 Same as Fig. 3, but for g'-band images. Small systemic offsets of ~ 0.05 mag on $(u' - g')$ are revealed.

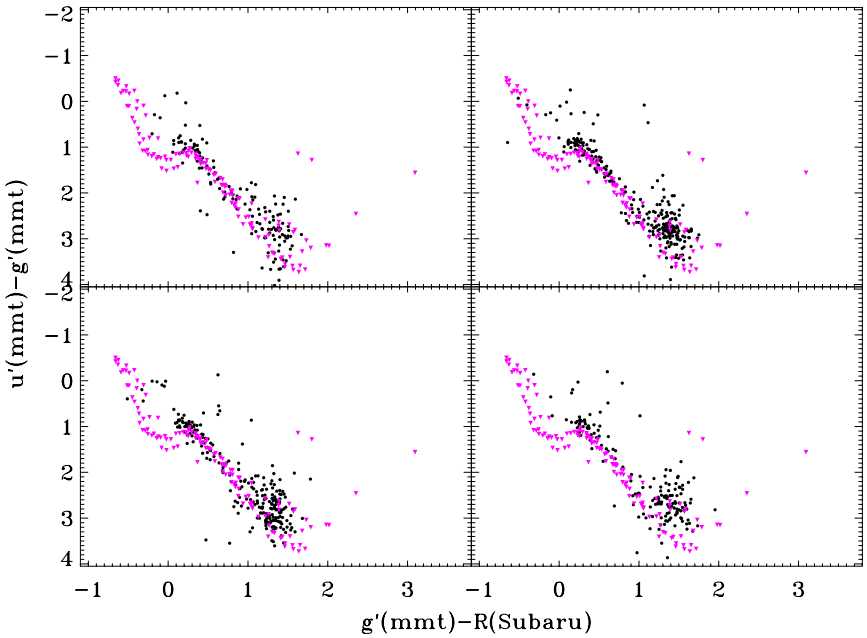

Fig. 5 Same as Fig. 3, but for R-band images. Although there exists a larger dispersion than the other two band figures, there are no obvious offsets between the observed and synthetic colors. We have corrected the zero point errors for the g'-band magnitudes when plotting this figure.

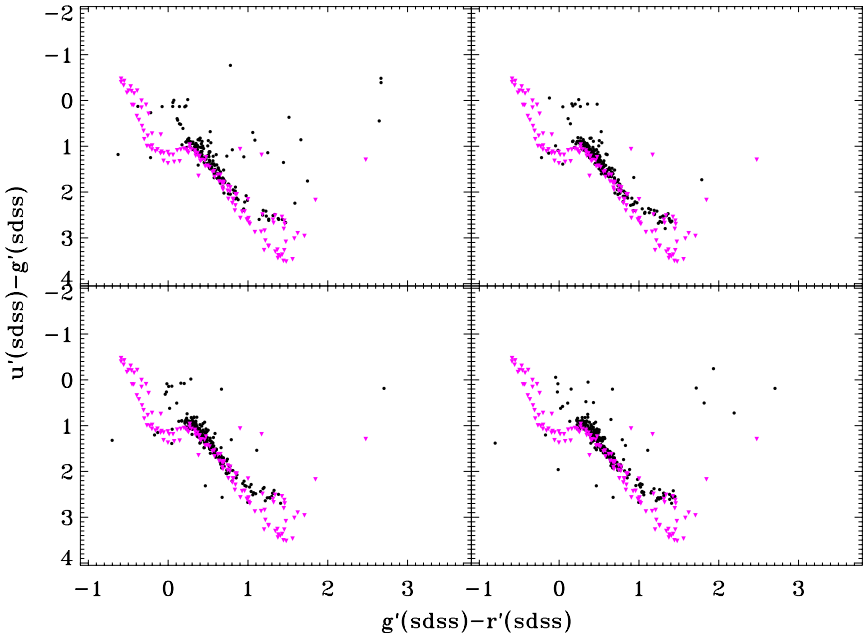

Fig. 6 Same as Fig. 3, but for SDSS $u'g'r'$ filters.

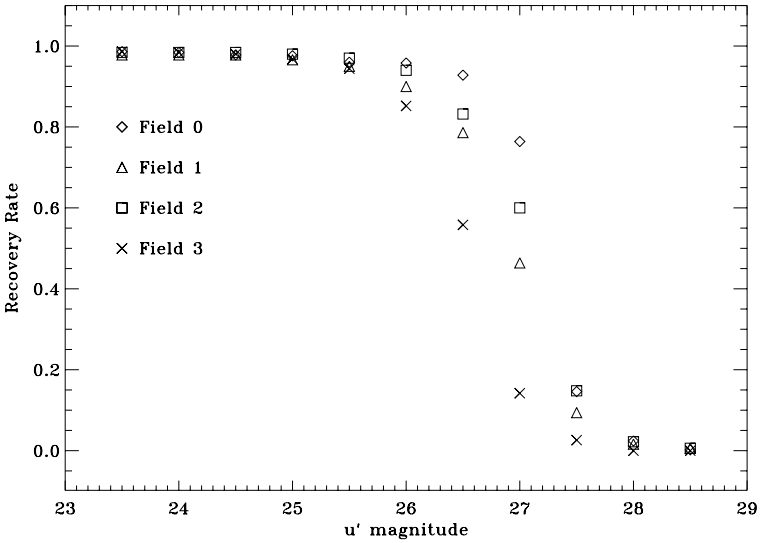

Fig. 7 Recovery rates versus magnitudes plotted for the u'-band images.

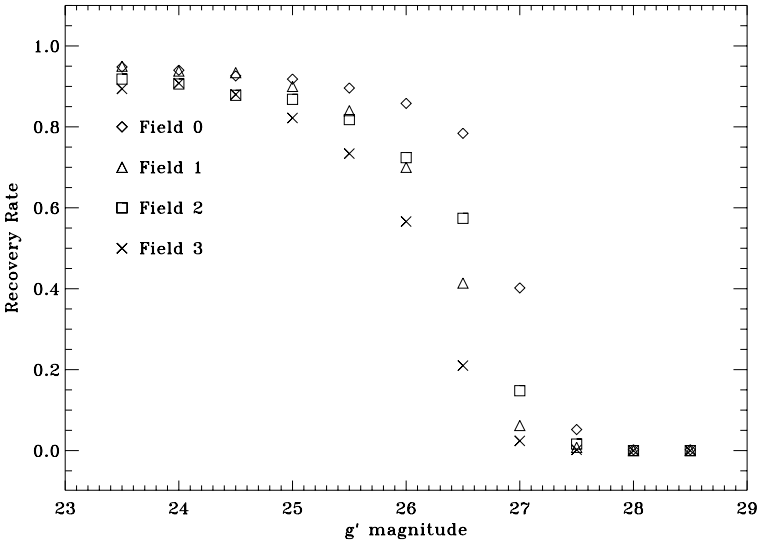

Fig. 8 Same as Fig. 7, but for the g'-band images.

3.1.1 Star-galaxy separation

Although SExtractor itself provides a parameter, CLASS_STAR [with values between 1 (starlike object) and 0], to separate starlike sources from extended sources, we use the half-light radius vs magnitude plot (as shown in Fig. 2) to separate stars from galaxies. This allows us to weed out saturated sources simultaneously, but this selection criterion does not work with sources fainter than 23.5 mag. However, number counts tend to be dominated by galaxies at the faint end. Therefore, we do not attempt to separate stars from galaxies at these flux levels.

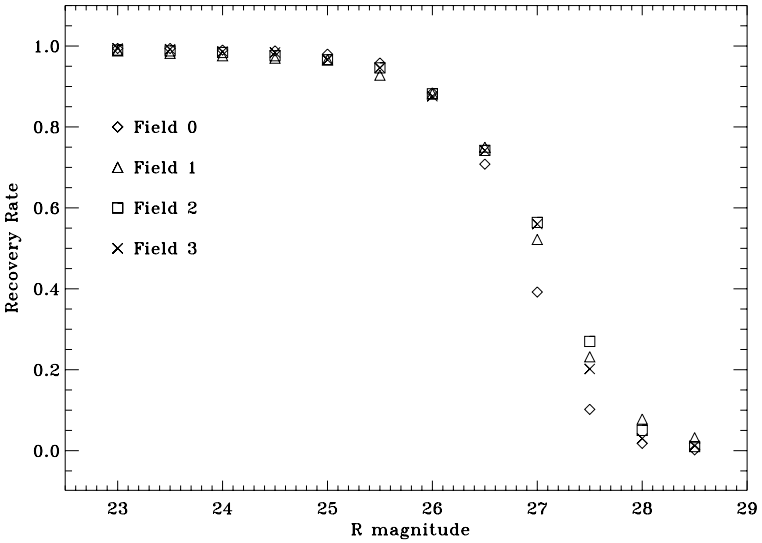

Fig. 9 Same as Fig. 7, but for the R-band images.

3.1.2 u'-band counts

The differential u'-band galaxy counts are plotted in Figure 10, with a compilation of published galaxy counts at close bands, e.g. Johnson/Kron U, CFHT u^*. All magnitudes have been converted to the SDSS AB magnitudes, using the conversion relation of galaxy colors from Fukugita et al. (1995). We can see that our results are very consistent with the other counts, except for those of Songaila et al. (1990), which have relatively lower values than all of the others. Meanwhile, the depth of the survey is deeper than that of CFHT. At the bright end ($u' \leq 20.5$), our counts have a relatively lower values than the others. This is believed to be due to the small number of galaxies detected in the field. A small divergency of the number of detected bright galaxies can result in a large variance of the mean counts. Within the range $21.75 \leq u' \leq 25.75$, the counts have a slope of $\mathrm{d}(\log N)/\mathrm{d}m_{u'} \sim 0.48$. As shown in the figure, our u'-band imaging is one of the deepest ground-based observations so far. Table 2 gives our u'-band counts.

3.1.3 g'-band counts

We show the g'-band counts in Figure 11, compiled with the results of the g'-band from SDSS (Yasuda et al. 2001), the B-band from the ground-based observations, and the $F450$-band from HDF north and south fields. It can be seen that our observation is deeper than most of the ground-based observations, but much shallower than the Hubble Space Telescope observations. The average slope $\mathrm{d}(\log N)/\mathrm{d}m$ is 0.4 for $20 \leq g' \leq 25.5$. The shallower slope, fainter than 25.5, is caused by incompleteness. However, it is also within 3σ at ~ 26.0 mag. Our g'-band counts are listed in Table 3.

3.1.4 R-band counts

In Figure 12, we plot the R-band counts. The SDSS' r' counts (Yasuda et al. 2001) and $F606$ counts on HDF north and south fields (Metcalfe et al. 2001) are also included, as well as other ground-based R-band observations. Our result agrees with the others very well. We can see that our observation is almost the deepest ground-based R-band observations up to now (up to ~ 26.5 mag); it is much deeper than CFHT's, and only the counts presented by Kashikawa et al. (2004) are comparable with ours. The counts

Table 2 Differential Galaxy Counts from the EGS Field in the u'-band

Magnitude (AB)	Number of Galaxies	Area (deg^2)	$\log N_{u'}$ (0.5 mag^{-1} deg^2)
19.75	11	0.25	1.642
20.25	15	0.25	1.777
20.75	43	0.25	2.234
21.25	73	0.25	2.464
21.75	143	0.25	2.756
22.25	261	0.25	3.017
22.75	523	0.25	3.319
23.25	1093	0.25	3.639
23.75	2151	0.25	3.933
24.25	3454	0.25	4.139
24.75	5539	0.25	4.344
25.25	7490	0.25	4.475
25.75	9032	0.25	4.556
26.25	9130	0.25	4.561
26.75	7525	0.25	4.477
27.25	4438	0.25	4.248
27.75	1461	0.25	3.765
28.25	188	0.25	2.875
28.75	36	0.25	2.157

Table 3 Differential Galaxy Counts from the EGS Field in the g'-band

Magnitude (AB)	Number of Galaxies	Area (deg^2)	$\log N_{g'}$ (0.5 mag^{-1} deg^2)
19.25	14	0.10	2.105
19.75	18	0.10	2.246
20.25	29	0.10	2.475
20.75	54	0.10	2.735
21.25	92	0.10	2.957
21.75	151	0.10	3.150
22.25	297	0.10	3.457
22.75	404	0.10	3.599
23.25	789	0.10	3.902
23.75	1327	0.10	4.112
24.25	1889	0.10	4.271
24.75	2685	0.10	4.424
25.25	3522	0.10	4.537
25.75	4135	0.10	4.603
26.25	4067	0.10	4.598
26.75	3339	0.10	4.501
27.25	1698	0.10	4.205
27.75	414	0.10	3.600
28.25	48	0.10	2.674

continue to increase, with an average slope of 0.36 for $20 \leq R \leq 26$ mag, but with evidence of a change to a somewhat shallower slope faintward of this. This apparent turnover is due to incompleteness. The results for the R-band are given in Table 4.

3.2 $u'g'R$ Photometric Selection of Lyman Break Galaxies

Various filter sets have yielded success at finding LBGs, such as $U_nG\mathcal{R}$ (Steidel et al. 1996), $G\mathcal{R}i$ (Steidel et al. 1999), BRI (Gawiser et al. 2001; Prochaska et al. 2002), SDSS $u'g'r'i'z'$ (Bentz et al. 2004), $u'BVRI$ (Cooke et al. 2005), and BVR (Gawiser et al. 2006). Figure 13 shows the difference

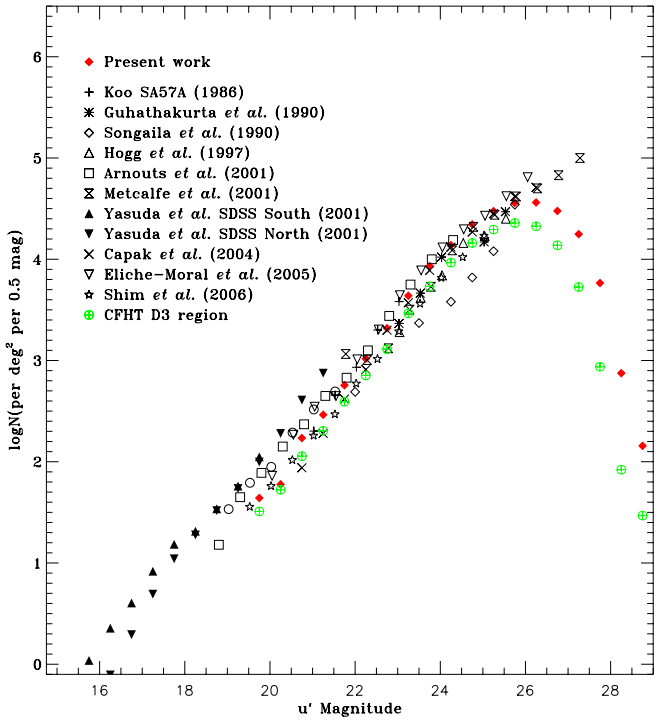

Fig. 10 u'-band differential counts compilation. Magnitudes are in the AB system.

in expected colors of model star-forming galaxies between our filter system and Steidel's filter system, with a variety of assumed redshifts and reddening by dust. There is no obvious difference between the $(u'-g')$ colors in $0.0 \leq (u'-g') \leq 1.0$. However, there exists a large discrepancy when $(u'-g') > 1$, which is the color range for almost all of the LBG candidates. For the case of the $(g'-R)$ color, there exists a strong correlation between color difference, $\Delta(g'-R) = (g'-R) - (G-\mathcal{R})$ and the $(g'-R)$ color. We use a minimum χ^2 fit to obtain: $\Delta(g'-R) = -0.01 - 0.16(g'-R)$. However, it is too complicated to transform the Steidel et al. criteria to our filter system. Hence, we generated our own color selection criteria. In Figure 14, we show the expected colors (through our filter system) versus redshifts of model star-forming galaxies with a variety of assumed reddening by dust. We also plotted the expected and the observed star colors and our adopted color selection criteria of

$$\begin{gathered} u'-g' \geq 1.8(g'-R)+0.9, \\ 0.0 \leq g'-R \leq 1.2, \\ 19.0 \leq R \leq 25.0, \end{gathered}$$

where all magnitudes are in AB. Since our observations (g'-band) are not as deep as Steidel's, we select LBGs up to $R = 25.0$ mag. In order to avoid contamination from the upper branch of the stellar distribution at red colors, we shifted our criteria to avoid this region as it also contains dim dwarf stars with correspondingly large errors in color, which are the primary expected source of interlopers. The region of the Steidel et al. (2003) criteria, which was avoided by this shift, had the highest fraction of interlopers.

In order to obtain accurate colors of the sources, we need to measure the flux within an aperture with the same size, assuming that the PSFs are nearly same. However, the PSFs are very different for our $u'g'R$-band images since they were obtained by using different detectors and under very different weather conditions (see Table 1). The seeing of the g'-band is always almost twice as big as that of the

Table 4 Differential Galaxy Counts from the EGS Field in the R-band

Magnitude (AB)	Number of Galaxies	Area (deg^2)	$\log N_R$ ($0.5\ mag^{-1}\ deg^2$)
19.25	35	0.20	2.248
19.75	86	0.20	2.639
20.25	146	0.20	2.869
20.75	228	0.20	3.062
21.25	424	0.20	3.332
21.75	585	0.20	3.471
22.25	961	0.20	3.687
22.75	1399	0.20	3.850
23.25	2095	0.20	4.025
23.75	3204	0.20	4.210
24.25	4884	0.20	4.393
24.75	6982	0.20	4.548
25.25	10086	0.20	4.708
25.75	13644	0.20	4.839
26.25	18712	0.20	4.976
26.75	23558	0.20	5.076
27.25	28233	0.20	5.155
27.75	21537	0.20	5.037
28.25	5773	0.20	4.466

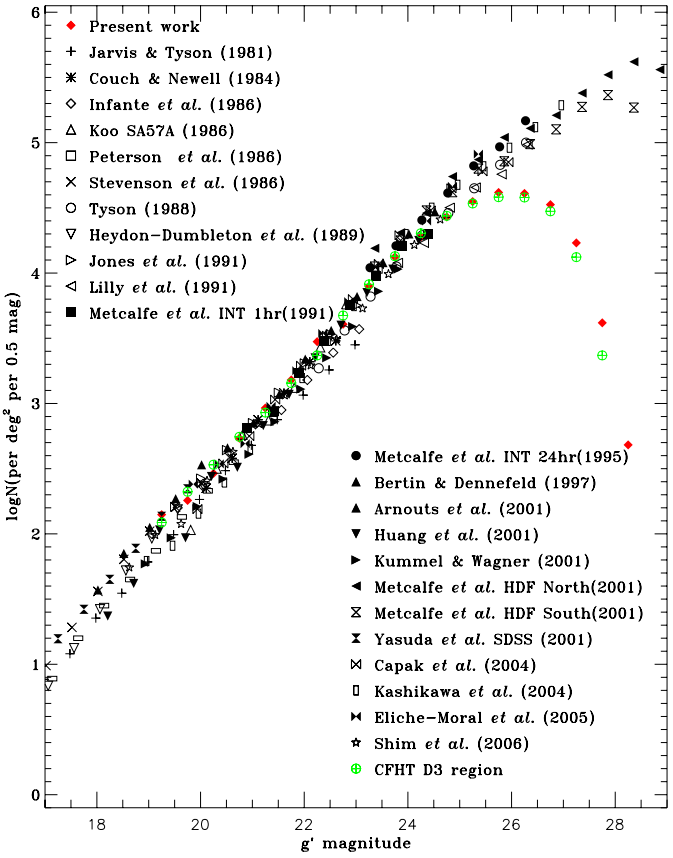

Fig. 11 g'-band differential count compilation, magnitudes are in the AB system.

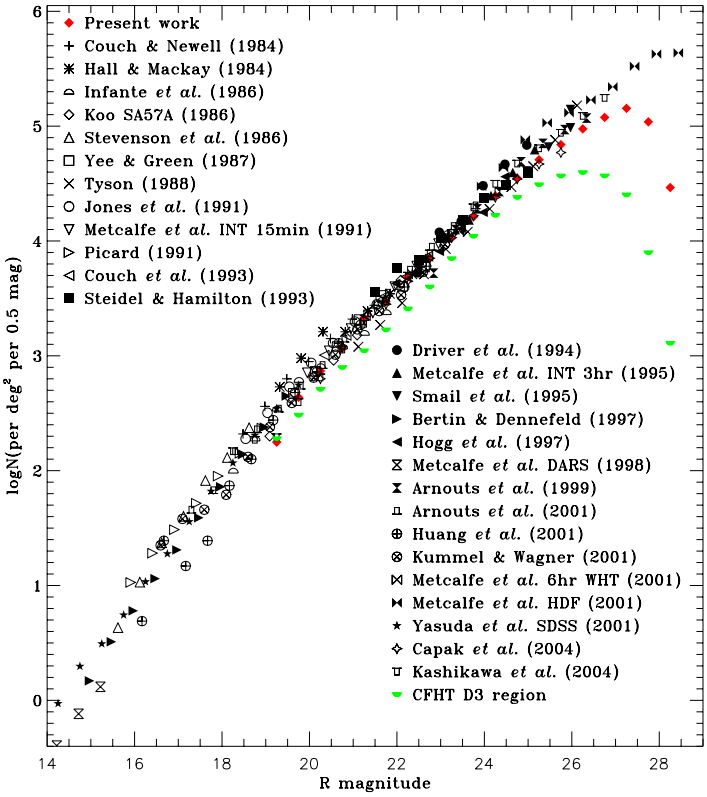

Fig. 12 R-band differential counts compilation, magnitudes are in the AB system. We can see that our depth at this band is much deeper than the CFHT's.

R-band. In Figure 15, we show the curve of growth for stars in Field 1. We can see that the profiles between the R-band and the u'- and g'-bands are very different. Furthermore, these profiles are non-Gaussian, and can be fitted by a Moffat function well. Hence, we do not simply use a Gaussian kernel to convolve the u'- and R-band images to match the g'-band images, but to deconvolve the g'-band PSF at first, then to convolve the original u'- and R-band images using the deconvolved kernels. The detection of objects was performed on the original rebinned R-band image, not the smoothed image, by using the Source Extractor's double-image mode. Objects were thought to be detected if the number of connected pixels with flux exceeding 3 times the sky σ is larger than 4. However, this has little effect on our results, since our cut off magnitude of R is 25.0 mag. The aperture size we chose is a $3''$ diameter circular aperture, to match the IRAC aperture size. The total R-band magnitude is measured on the original image by using a same size aperture, which can include almost all the light from a point source, as shown in the growth curve in Figure 15.

Since many sources are undetected in the u'-band image, objects with u' flux, $f_{u'}$, less than their 1σ flux uncertainty, $\sigma_{u'}$, are assigned an upper limit of $f_{u'} = \sigma_{u'}$, where $\sigma_{u'} = N_{\rm pix}^{0.5}\sigma_{\rm sky}$, and $N_{\rm pix}$ is the number of pixels in the detection aperture and $\sigma_{\rm sky}$ is the rms pixel-to-pixel fluctuations in the sky background. This procedure is the same as Steidel et al. (2003). The limiting values are used to generate the $(u'-g')$ colors. Our selection criteria yield 1642 candidates in 1637.3 arcmin^2, as listed in Table 5. When making the LBG selections, we have trimmed the images of Field 0, Field 2 and Field 3, according to the signal-to-noise ratio. The average surface density of the candidates is ~ 1.0 galaxies arcmin^{-2}, which is slightly higher than that of ~ 0.9 galaxies arcmin^{-2} (at $R_{\rm AB} = 25.0$ mag), found

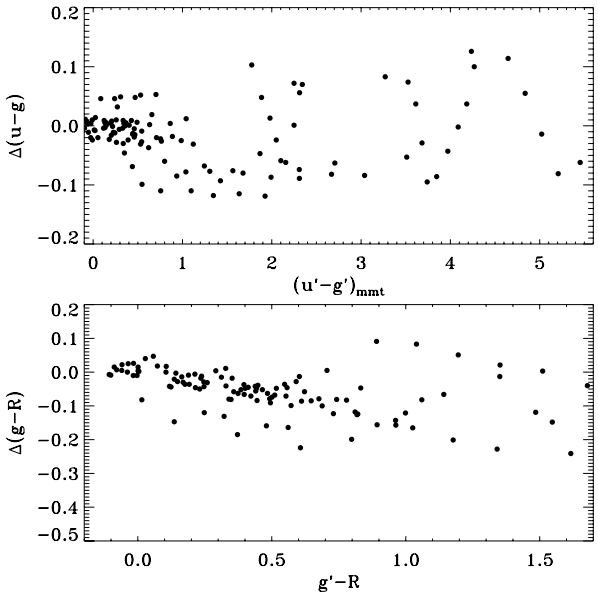

Fig. 13 Dependence of color difference between our filter system and the filter system used by Steidel, on our color. We can see a strong correlation in the bottom panel.

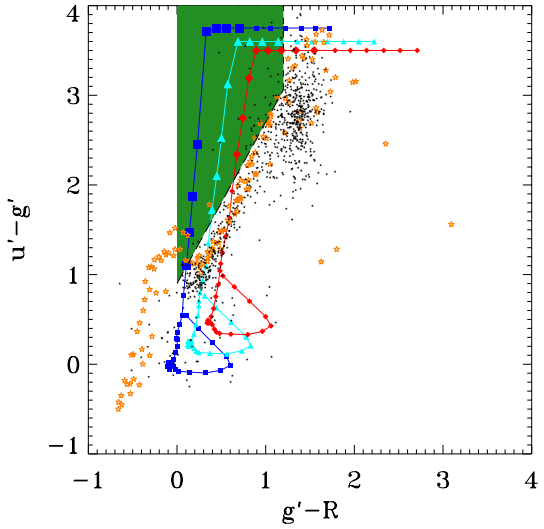

Fig. 14 $(u' - g')$ vs. $(g' - R)$ colors in our filter system (AB magnitudes) of a star-forming galaxy with a constant star formation rate in the targeted redshift range, for three assumed values of internal extinction [$E(B - V) = 0$, 0.15, 0.30 using the Calzetti et al. 2000 prescription, for squares, triangles, and diamonds, respectively], with points corresponding to intervals of $\Delta z = 0.1$. The large points on each curve correspond to galaxies in the redshift interval $2.7 \leq z \leq 3.4$. The $(u' - g')$ colors have been truncated for clarity. The expected location of the stellar locus, based on the stellar spectral library HILIB (Pickles 1998), is shown with orange stars. The observational stellar colors are shown with black stars. The green shaded region shows our adopted color selection criteria.

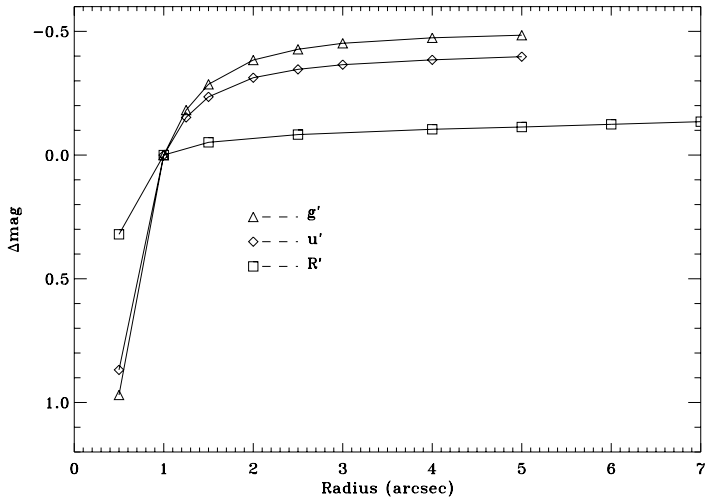

Fig. 15 Growth curve of stars for u'-, g'-and R-band images in Field 1.

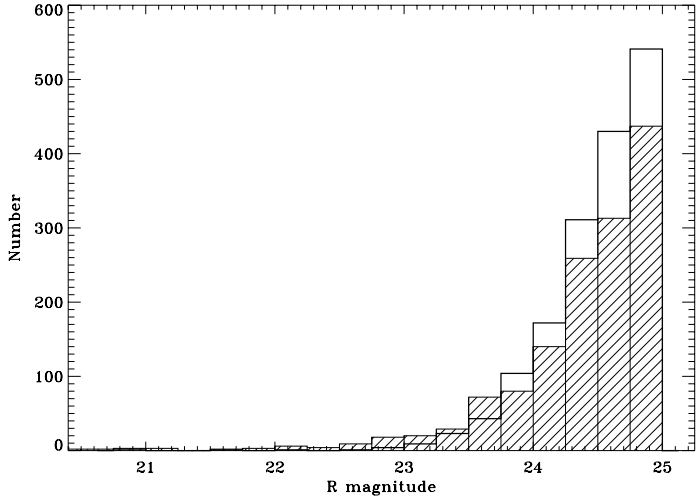

Fig. 16 Magnitude distributions of the full photometric LBG sample with $19.0 \leq R_{\rm AB} \leq 25.0$ (*thick line*). We only plot up to $R \geq 20.5$ since there are no LBGs brighter than 20.5 mag in the sample. It can be seen that this distribution is consistent with that (*hashed histogram*) in Steidel et al. (2003).

by Steidel et al. (2003). We believe that this discrepancy is mainly caused by the observational depth and/or the cosmic variance.

Figure 16 shows the magnitude distribution of the full photometrically selected LBG sample [4]. It is very similar to that shown in Steidel et al. (2003). Most LBG candidates are dim sources, and we found no LBGs brighter than 20.5 mag in this sample. In subsequent papers of this series, we will present the properties for the LBG sample, such as photometric redshift, stellar mass, and the feature of clustering.

[4] This catalog has been updated since new data were obtained.

Table 5 LBG Candidates Selected in the Four EGS Fields

Field	Area (arcmin^2)	Number	Surface density (arcmin^{-2})
0	240.4	195	0.8
1	916.4	1020	1.1
2	153.0	167	1.1
3	327.4	260	0.8
Total	1637.3	1642	1.0

4 SUMMARY

In this paper, we present the photometry for the Extended Groth Strip $u'g'R$ survey, assembled by using the MMT/Megacam and the Subaru/Suprime. This paper describes in detail the photometric calibration, limiting magnitudes and galaxy number counts. The galaxy number counts are consistent with previous results. The number counts show that our u'-band observation is one of the deepest ground-based observations so far, and our g'-band observation is deeper than most of the ground-band observations. The counts also show that our R-band observation reaches $26.2 \sim 26.5$ mag, which allows our observation to be the deepest ground-based observation up to now. These also mean that our observations are deep enough to study the high redshift and consequently dim objects.

We also present a photometrically selected LBG sample as the first scientific result. The high quality of the R-band images may resolve high redshift objects and allow us to study their structures. In subsequent papers of this series, we will present some other scientific results for the LBG sample.

Acknowledgements The observations reported here were obtained in part at the MMT Observatory, a facility operated jointly by the Smithsonian Institution and the University of Arizona. Y. H. ZHAO would like to gratefully acknowledge financial support from the China Scholarship Council (CSC), the Jiangsu Planned Projects for Postdoctoral Research Funds (No. 0802031C) and the K.C. Wong Education Foundation, Hong Kong.

References

Arnouts, S., D'Odorico, S., Cristiani, S., Zaggia, S., Fontana, A., & Giallongo, E. 1999, A&A, 341, 641
Arnouts, S., et al. 2001, A&A, 379, 740
Barmby, P., et al. 2004, ApJS, 154, 97
Bentz, M. C., Osmer, P. S., & Weinberg, D. H. 2004, ApJ, 600, L19
Bertin, E., & Arnouts, S. 1996, A&AS, 117, 393
Bertin, E., & Dennefeld, M. 1997, A&A, 317, 43
Calzetti, D., Armus, L., Bohlin, R. C., Kinney, A. L., Koornneef, J., & Storchi-Bergmann, T. 2000, ApJ, 533, 682
Capak, P., et al. 2004, AJ, 127, 180
Cooke, J., Wolfe, A. M., Prochaska, J. X., & Gawiser, E. 2005, ApJ, 621, 596
Couch, W. J., Jurcevic, J. S., & Boyle, B. J. 1993, MNRAS, 260, 241
Couch, W. J., & Newell, E. B. 1984, ApJS, 56, 143
Daddi, E., et al. 2004, ApJ, 617, 746
Davis, M., et al. 2007, ApJ, 660, L1
Dickinson, M., et al. 2004, ApJ, 600, L99
Driver, S. P., Phillipps, S., Davies, J. I., Morgan, I., & Disney, M. J. 1994, MNRAS, 268, 393
Eliche-Moral, C., Balcells, M., Prieto, M., & Cristóbal-Hornillos, D. 2005, RMxAC, 24, 237
Elsner, F., Feulner, G., & Hopp, U. 2008, A&A, 477, 503
Fazio, G. G., et al. 2004, ApJS, 154, 10
Franx, M., Labbe, I., Rudnick, G., van Dokkum, P. G., et al. 2003, ApJ, 587, 79
Fukugita, M., Ichikawa, T., Gunn, J. E., Doi, M., Shimasaku, K., & Schneider, D. P. 1996, AJ, 111, 1748
Fukugita, M., Shimasaku, K., & Ichikawa, T. 1995, PASP, 107, 945

Gawiser, E., et al. 2006, ApJS, 162, 1
Gawiser, E., Wolfe, A. M., Prochaska, J. X., Lanzetta, K. M., Yahata, N., & Quirrenbach, A. 2001, ApJ, 562, 628
Guhathakurta, P., Tyson, J. A., & Majewski, S. R. 1990, ApJ, 357, L9
Gunn, J. E., et al. 1998, AJ, 116, 3040
Hall, P., & Mackay, C. D. 1984, MNRAS, 210, 979
Heydon-Dumbleton, N. H., Collins, C. A., & MacGillivray, H. T. 1989, MNRAS, 238, 379
Hogg, D. W., Pahre, M. A., McCarthy, J. K., Cohen, J. G., Blandford, R., Smail, I., & Soifer, B. T. 1997, MNRAS, 288, 404
Huang, J.-S., et al. 2001, A&A, 368, 787
Huang, J.-S., et al. 2005, ApJ, 634, 137
Huang, J.-S., et al. 2007, ApJ, 660, L69
Infante, L., Pritchet, C., & Quintana, H. 1986, AJ, 91, 217
Jarvis, J. F., & Tyson, J. A. 1981, AJ, 86, 476
Jones, L. R., Fong, R., Shanks, T., Ellis, R. S., & Peterson, B. A. 1991, MNRAS, 249, 481
Kashikawa, N., et al. 2004, PASJ, 56, 1011
Koo, D. C. 1986, ApJ, 311, 651
Kümmel, M. W., & Wagner, S. J. 2001, A&A, 370, 384
Lehnert, M. D., & Bremer, M. 2003, ApJ, 593, 630
Lilly, S. J., Cowie, L. L., & Gardner, J. P. 1991, ApJ, 369, 79
Metcalfe, N., Ratcliffe, A., Shanks, T., & Fong, R. 1998, MNRAS, 294, 147
Metcalfe, N., Shanks, T., Camos, A., McCracken, H. J., & Fong, R. 2001, MNRAS, 323, 795
Metcalfe, N., Shanks, T., Fong, R., & Jones, L. R. 1991, MNRAS, 249, 498
Metcalfe, N., Shanks, T., Fong, R., & Roche, N. 1995, MNRAS, 273, 257
Miyazaki, S., et al. 2002, PASJ, 54, 833
Miyazaki, S., Hamana, T., Ellis, R. S., et al. 2007, ApJ, 669, 714
Monet, D. G., et al. 2003, AJ, 125, 984
Oke, J. B., & Gunn, J. E. 1983, ApJ, 266, 713
Ouchi, M., et al. 2004, ApJ, 611, 660
Peterson, B. A., Ellis, R. S., Efstathiou, G., Shanks, T., Bean, A. J., Fong, R., & Zen-Long, Z. 1986, MNRAS, 221, 233
Picard, A. 1991, ApJ, 102, 445
Pickles, A. J. 1998, PASP, 110, 863
Prochaska, J. X., Gawiser, E., Wolfe, A. M., Quirrenbach, A., Lanzetta, K. M., Chen, H., Cooke, J., & Yahata, N. 2002, AJ, 123, 2206
Rhodes, J., Refregier, A., & Groth, E. J. 2000, ApJ, 536, 79
Rieke, G. H., et al. 2004, ApJS, 154, 25
Rigopoulou, D., et al. 2006, ApJ, 648, 81
Sawicki, M., & Thompson, D. 2006, ApJ, 642, 653
Shapley, A. E., Steidel, C. C., Erb, D. K., Reddy, N. A., Adelberger, K. L., Pettini, M., Barmby, P., & Huang, J.-S. 2005, ApJ, 626, 698
Shim, H., Im, M., Pak, S., Choi, P., Fadda, D., Helou, G., & Storrie-Lombardi, L. 2006, ApJS, 164, 435
Smail, I., Hogg, D. W., Yan, L., & Cohen, J. G. 1995, ApJ, 449, L105
Songaila, A., Cowie, L. L., & Lilly, S. J. 1990, ApJ, 348, 371
Steidel, C. C., Adelberger, K. L., Giavalisco, M., Dickinson, M., & Pettini, M. 1999, ApJ, 519, 1
Steidel, C. C., Adelberger, K. L., Shapley, A. E., Pettini, M., Dickinson, M., & Giavalisco, M. 2003, ApJ, 592, 728
Steidel, C. C., Giavalisco, M., Pettini, M., Dickinson, M., & Adelberger, K. L. 1996, ApJ, 462, L17
Steidel, C. C., & Hamilton, D. 1993, AJ, 105, 2017
Stevenson, P. R. F., Shanks, T., & Fong, R. 1986, ASSL, 122, 439
Tyson, J. A. 1988, AJ, 96, 1
Werner, M. W., et al. 2004, ApJS, 154, 1
Yasuda, N., et al. 2001, AJ, 122, 1104
Yee, H. K. C., & Green, R. F. 1987, ApJ, 319, 28